ChemComm

COMMUNICATION

View Article Online
View Journal | View Issue

Cite this: *Chem. Commun.*, 2025, **61**, 19441

Received 4th September 2025,
Accepted 6th November 2025

DOI: 10.1039/d5cc05122c

rsc.li/chemcomm

Chemical defects as Li^+ ion traps: a theoretical study

Dong Yoon Shin, [ab] Jacek Kłos,[cd] Jacob Fortner[ab] and YuHuang Wang*[abe]

We investigate how sp^3 quantum defects on single-walled carbon nanotubes act as atomic-scale traps for individual lithium ions. Density functional theory (DFT) calculations show that endohedrally incorporated Li^+ in (7,5) single-walled carbon nanotubes preferentially localize near aryl-hydroxyl sp^3 defects, with a binding energy of ~2.95 eV. This defect-ion interaction redistributes local charge, perturbs frontier orbitals, and produces a 437 meV red-shift in the defect absorption spectrum, as revealed by time-dependent DFT. These findings highlight the sensitivity of quantum defects to ions, with implications for ion detection, quantum emitters, and lithium storage in carbon nanotube-based electrodes.

Carbon nanotubes (CNTs) are quasi-one-dimensional nanomaterials with wide-ranging applications in optoelectronics, catalysis, sensing, biomedicine, and energy storage.[1–3] Among these applications, their role in lithium-ion batteries has attracted particular attention, as CNTs can improve both storage capacity and electrical transport.[4–6] A fundamental understanding of how lithium ions interact with the carbon matrix at the atomic level is critical. Previous theoretical studies suggest that a Li^+ preferentially localizes near CNT sidewalls, where it perturbs the nanotube's electronic properties by inducing charge transfer from the CNT to the ion, shifting the Fermi level, and in some cases driving a semiconductor-to-metal transition through Li^+-induced gap states.[7–9]

Defects are known to dramatically alter CNT electrical and optical properties by introducing mid-gap states, shifting optical absorption and emission energies, and modifying local charge transport.[10–16] In particular, covalently installed sp^3 quantum defects, which are introduced through functionalization with organic functional groups,[12–16] generate exciton traps that give rise to defect photoluminescence (PL) in the shortwave infrared,[17] enabling applications in chemical sensing, ion detection, and biomedical imaging.[18–21] Defect sites have also been implicated in ion intercalation and transport in electrochemical systems.[22,23] However, despite their importance, the atomistic details of how defects interact with ions in general remain poorly understood. Addressing this knowledge gap is essential for advancing CNT-based materials in both sensing and energy storage technologies.

Herein, we investigate ion-defect interactions in sp^3-defect-tailored single-walled CNTs (SWCNTs) using density functional theory (DFT). We provide the first atomistic description of how a structurally defined sp^3 quantum defect acts as a strong trapping site for a single Li^+ inside the nanotube and how this interaction modulates the defect's electronic and optical properties. Using a (7,5) SWCNT functionalized with an sp^3 aryl-hydroxyl defect pair, we find that a Li^+ becomes trapped near the hydroxyl group. This ion trapping leads to pronounced changes in charge distribution, frontier orbital localization, and optical absorption. Time-dependent DFT predicts a 437 meV red-shift in the lowest-energy singlet transition upon ion trapping. These results show that even a single ion can drastically alter the electronic and optical properties of defect-sensors, and optoelectronic devices.

Each SWCNT structure is uniquely determined by its chiral vector, (n,m).[24] In this study, we used the (7,5) SWCNT as a model system to investigate ion-defect interactions. We selected the (7,5) SWCNT because it is an experimentally accessible system with well-characterized optical transitions and established sp^3 functionalization chemistry, providing an ideal model system for elucidating the ion-trapping mechanism at a single defect site. The nanotube was modeled as a finite, ~4.5 nm-long segment (one pristine unit cell), with dangling bonds passivated by hydrogen and methylene groups to minimize edge effects.[25] A quantum defect was introduced by

[a] *Department of Chemistry and Biochemistry, University of Maryland, College Park, Maryland 20742, USA. E-mail: yhw@umd.edu*
[b] *Chemical Physics Program, Institute for Physical Science and Technology, University of Maryland, College Park, Maryland 20742, USA*
[c] *Department of Physics, University of Maryland, College Park, Maryland 20742, USA*
[d] *Joint Quantum Institute, University of Maryland, College Park, Maryland 20742, USA*
[e] *Maryland NanoCenter, University of Maryland, College Park, Maryland 20742, USA*

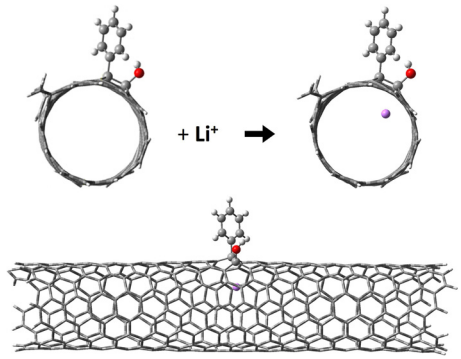

Fig. 1 Optimized geometry of a Li^+ at a defect trap featuring a pair of aryl and OH (Ar-OH) sp^3 defects in a (7,5) SWCNT. The Li^+ was found to preferentially localize near the OH group of the defect.

covalently attaching an aryl ($-C_6H_5$) and hydroxyl ($-OH$) pair to the nanotube surface, as typically observed experimentally.[26] A Li^+ was then inserted into the pore of the (7,5) SWCNT-Ar-OH system.

All DFT calculations were performed using the Gaussian software packages[27,28] (see SI for details). After constructing the pristine and defective nanotubes, full geometry optimizations were carried out (Fig. S1). For ion-defect systems, a Li^+ was initially placed along the nanotube center line at multiple positions, followed by geometry optimization to locate minimum-energy configurations. This procedure allowed us to determine whether a Li^+ preferentially binds near the quantum defect and to evaluate how its position influences the stability and electronic structure of the system.

Geometry optimizations consistently showed that Li^+ prefers to localize near the hydroxyl group of the Ar-OH defect. Supplementary calculations from multiple starting geometries (Fig. S2) identified four local minima, all clustered around the OH group. The lowest-energy configuration, shown in Fig. 1, features Li^+ stabilized adjacent to the OH group, highlighting the decisive role of electrostatic interactions in defining the trapping site.

We calculated the ion-defect binding energy (E_b) using the following equation:

$$E_b = E_{SWCNT\text{-}Ar\text{-}OH} + E_{Li^+} - E_{SWCNT\text{-}Ar\text{-}OH+Li^+} \quad (1)$$

where $E_{SWCNT\text{-}Ar\text{-}OH}$, E_{Li^+}, and $E_{SWCNT\text{-}Ar\text{-}OH+Li^+}$ are the total energies of the (7,5) SWCNT-Ar-OH, the Li^+, and the entire system of the (7,5) SWCNT-Ar-OH with the inserted Li^+, respectively. The binding energy of Li^+ near the defect was calculated as 2.945 eV, compared to $\sim$2.80 eV inside a pristine (7,5) SWCNT without a defect. For reference, our calculated Li^+ binding energy on the pristine SWCNT ($\sim$2.80 eV) agrees well with previously reported theoretical values for Li^+ interactions with pristine SWCNTs, which typically fall in the range of 2.5–3.0 eV.[7,8] This enhancement of 0.12–0.15 eV demonstrates that the defect acts as a preferential ion trap. Along the nanotube axis, the defect introduces a clear energy minimum (Fig. 2b), whereas in pristine tubes, the binding energy remains nearly constant (Fig. 2a). To further assess the confinement of the ion, bound vibrational states of the Li^+ were evaluated with a discrete variable representation[29] using the polynomial fit of

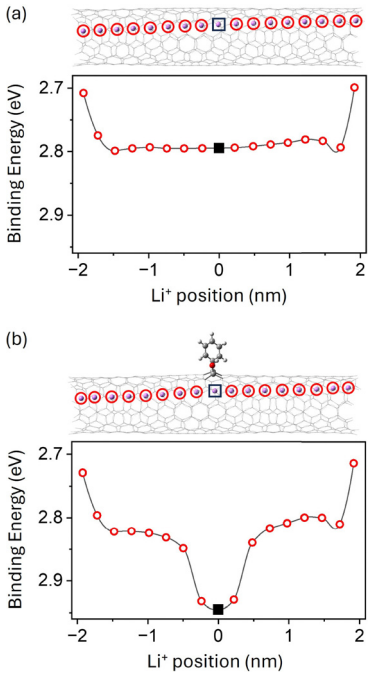

Fig. 2 Binding energy of a Li^+ to the ion trap. Binding energy of a Li^+ along the tube axis in a (7,5) SWCNT (a) without and (b) with an Ar-OH quantum defect trap. A clear binding-energy maximum appears near the defect site, confirming ion trapping.

the binding energy as a function of the ion's displacement from edge to edge of the CNT. The results (Fig. S3) suggest that the Li^+ is dynamically confined within a potential well shaped by the localized defect.

The positive electric charge of the Li^+ causes changes in the electronic properties of the (7,5) SWCNT-Ar-OH system. Natural Bond Orbital (NBO) population analysis shows that carbons near the Li^+ change from positive to negative partial charges, while the sp^3-defect carbons, which are connected to the aryl and hydroxyl functional groups, become more positive (Fig. 3). This redistribution reflects electron withdrawal by the Li^+ and modifies the local electrostatic potential and electron density around the defect, as illustrated in Fig. 4 using the GaussView

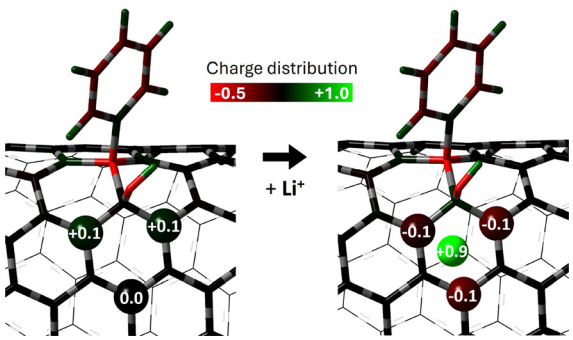

Fig. 3 Li^+-induced charge redistribution at a SWCNT defect. NBO charge distribution of the (7,5) SWCNT-Ar-OH with and without a trapped Li^+. Carbons adjacent to the ion shift from positive to negative partial charges, while defect carbons become more positive.

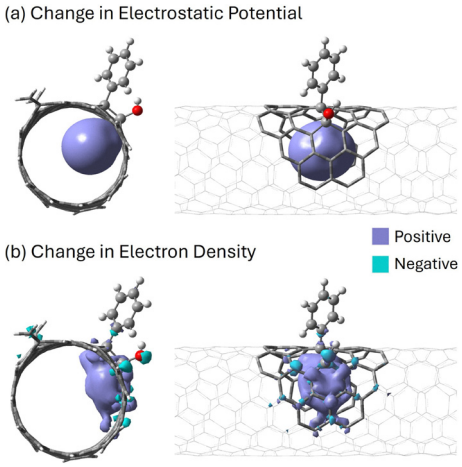

Fig. 4 Electrostatic potential and electron density maps showing redistribution induced by a trapped Li^+ at the defect. A Li^+ changes the spatial distribution of the (a) electrostatic potential and (b) electron density around the defect in (7,5) SWCNT-Ar-OH. The change in electrostatic potential was plotted at the isovalue of 0.1, and the change in electron density was plotted at the isovalue of 0.001. The trapped Li^+ generates a localized positive potential and enhanced electron density near the defect. These changes show that the Li^+ is drawing electrons from the nanotube sidewall.

program.[30] Quantitatively, NBO analysis reveals a net transfer of $\sim 0.1e$ from the defect carbons to the Li^+, leaving the carbons slightly electron-deficient (+0.1 e) and the Li^+ ion partially neutralized (+ 0.9*e*, relative to + 1.0*e* for a free ion).

Beyond electrostatic potential changes, the presence of a Li^+ also alters the nanotube's electronic structure at the orbital level. Fig. 5 presents the Kohn–Sham orbitals obtained from the DFT calculations. In the pristine nanotube, both the highest occupied molecular orbital (HOMO) and the lowest unoccupied molecular orbital (LUMO) are delocalized across the system. However, introducing a Li^+ causes the LUMO to localize around the defect and the HOMO to shift to the nanotube ends. This edge-weighted HOMO density is due to edge states and not intrinsic to pristine nanotubes; with hydrogen and methylene groups passivation, this artifact is reduced (Fig. S1), and our conclusions rest on the defect-localized LUMO and binding-energy profile, which are robust against the edge effects. This re-partitioning of frontier electronic states is driven by the local positive field of the Li^+, which electrostatically polarizes the π-system. This polarization, in turn, produces electron accumulation on the carbons nearest the ion (Fig. 3) and a more positive potential at the defect site (Fig. 4). This redistribution stabilizes the defect-centered LUMO and leads to the pronounced red-shift in the optical transition, as detailed below.

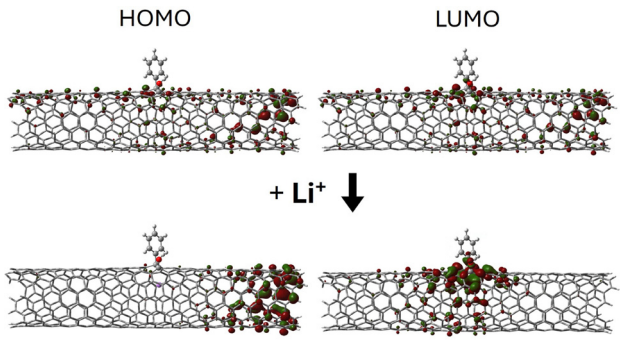

Fig. 5 Kohn–Sham orbitals of the (7,5)-SWCNT-Ar-OH system with a trapped Li^+. Surfaces of the HOMO and LUMO of the (7,5) SWCNT-Ar-OH with and without the Li^+ were plotted at an isovalue of 0.02. The LUMO localizes near the defect upon ion trapping, while the HOMO shifts toward the tube ends. This orbital re-partitioning is consistent with preferential LUMO stabilization by the Li^+-induced local electric field, which narrows the HOMO–LUMO gap.

Time-dependent DFT calculations reveal a strong optical response to Li^+ trapping. The simulated absorption spectra (Fig. 6) show that the defect transition red-shifts from 1092 nm (1.135 eV) to 1776 nm (0.6982 eV), corresponding to a 437 meV (38.5%) decrease in transition energy. Supplementary calculations performed with multiple basis sets (STO-3G, 3-21G, 6-31G, and 6-31G*) confirm that this red-shift is robust (Table S4 and Fig. S4). Importantly, this single-ion-induced red-shift is significantly larger than the spectral changes typically observed from solvent or dielectric screening effects in SWCNTs, suggesting exceptional sensitivity of the defect optical signature to nearby ions. Although these calculations were performed in vacuum, the surrounding dielectric environment is expected to further modulate this optical response. These findings demonstrate that the electronic and optical properties of a SWCNT can be influenced by the endohedral Li^+. While Li^+ was used here as a representative ion, we speculate the underlying mechanism is general and extendable to other ions, motivating our ongoing, broader investigations.

In summary, we show that sp^3 quantum defects in SWCNTs act as atomic-scale traps for Li^+, strongly modifying charge distribution, orbital localization, and optical transitions. Geometry optimization reveals that a Li^+ is preferentially stabilized near the hydroxyl group of the defect, with a binding energy of 2.945 eV, compared to ~2.80 eV in pristine nanotubes. The ion trapping depletes electron density from the nanotube, resulting in a more positive electrostatic potential around the defect and reshaping the frontier orbitals of the nanotube. Time-

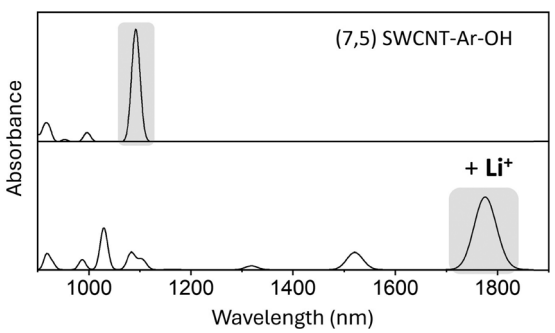

Fig. 6 Spectral response to the Li^+. Time-dependent DFT simulated absorption spectra featuring the ten lowest singlet excitonic transitions for the (7,5) SWCNT-Ar-OH with and without the Li^+. The trapped ion induces a red-shift of 437 meV in the lowest singlet transition, from 1092 nm (without the Li^+) to 1776 nm (with the Li^+).

dependent DFT predicts a pronounced 437 meV red-shift in the defect-associated optical transition upon Li^+ trapping. To our knowledge, this is the first theoretical prediction of Li^+ trapping at a chemically defined quantum defect in a SWCNT. Although direct experimental observation of a single ion bound to a specific defect has not yet been reported, our calculations provide a concrete and testable prediction for future studies. Advances in single-defect spectroscopy[31] and controlled endohedral filling,[32,33] may enable direct experimental verification of the predicted ion-induced spectral shifts at individual defect sites.

These results establish an atomistic mechanism for Li^+ trapping at chemically engineered defect sites, providing insight into lithium storage and transport in CNT-based electrodes, with implications for tuning capacity, transport, and stability in energy storage systems. More broadly, our findings highlight a generalizable mechanism by which single ions can strongly modulate quantum-defect photophysics, suggesting opportunities for CNT-based ion sensors, tunable quantum emitters, and ion-responsive optoelectronic devices.

We gratefully acknowledge the Maryland Advanced Research Computing Center (MARCC) and the University of Maryland supercomputing resources (**https://hpcc.umd.edu**) for providing the computational resources for the quantum chemical calculations. This work was supported in part by the Center for Enhanced Nanofluidic Transport (CENT), an Energy Frontier Research Center funded by the U.S. Department of Energy, Office of Science, Basic Energy Sciences under Award DE-SC0019112.

Conflicts of interest

There are no conflicts to declare.

Data availability

The data supporting this article are included in the Supplementary information (SI). Supplementary information is available. See DOI: **https://doi.org/10.1039/d5cc05122c**.

Notes and references

1 A. de Juan, Y. Pouillon, L. Ruiz-Gonzalez, A. Torres-Pardo, S. Casado, N. Martin, A. Rubio and E. M. Perez, *Angew. Chem., Int. Ed.*, 2014, **53**, 5394–5400.
2 J. M. Schnorr and T. M. Swager, *Chem. Mater.*, 2010, **23**, 646–657.
3 M. F. L. De Volder, S. H. Tawfick, R. H. Baughman and A. J. Hart, *Science*, 2013, **339**, 535–539.
4 Q. Xiao, Y. Fan, X. Wang, R. A. Susantyoko and Q. Zhang, *Energy Environ. Sci.*, 2014, **7**, 655.
5 C.-F. Sun, K. Karki, Z. Jia, H. Liao, Y. Zhang, T. Li, Y. Qi, J. Cumings, G. W. Rubloff and Y. Wang, *ACS Nano*, 2013, **7**, 2717–2724.
6 P. Wang, B. Barnes, Z. Huang, Z. Wang, M. Zheng and Y. Wang, *Adv. Mater.*, 2021, **33**, 2005890.
7 O. M. Korsun, O. N. Kalugin and O. V. Prezhdo, *J. Phys. Chem. Lett.*, 2014, **5**, 4129–4133.
8 O. M. Korsun, O. N. Kalugin, A. S. Vasenko and O. V. Prezhdo, *J. Phys. Chem. C*, 2016, **120**, 26514–26521.
9 V. Meunier, J. Kephart, C. Roland and J. Bernholc, *Phys. Rev. Lett.*, 2002, **88**, 075506.
10 P. G. Collins, in *Oxford Handbook of Nanoscience & Technology*, ed. A. V. Narlikar and Y. Y. Fu, Oxford Univ. Press, 2010, 31–93.
11 T. Biktagirov, U. Gerstmann and W. G. Schmidt, *Nanoscale*, 2025, **17**, 6884–6891.
12 A. H. Brozena, M. Kim, L. R. Powell and Y. Wang, *Nat. Rev. Chem.*, 2019, **3**, 375–392.
13 J. Fortner and Y. Wang, *J. Phys. Chem. Lett.*, 2022, **13**, 8908–8913.
14 P. Wang, J. Fortner, H. Luo, J. Kłos, X. Wu, H. Qu, F. Chen, Y. Li and Y. Wang, *J. Am. Chem. Soc.*, 2022, **144**, 13234–13241.
15 B. Eller, J. Fortner, J. Kłos, Y. Wang and C. W. Clark, *J. Phys.: Condens. Matter*, 2022, **34**, 464004.
16 M. Kim, X. Wu, G. Ao, X. He, H. Kwon, N. F. Hartmann, M. Zheng, S. K. Doorn and Y. Wang, *Chemistry*, 2018, **4**, 2180–2191.
17 Y. Piao, B. Meany, L. R. Powell, N. Valley, H. Kwon, G. C. Schatz and Y. Wang, *Nat. Chem.*, 2013, **5**, 840–845.
18 H. Kwon, M. Kim, B. Meany, Y. Piao, L. R. Powell and Y. Wang, *J. Phys. Chem. C*, 2015, **119**, 3733–3739.
19 T. Shiraki, H. Onitsuka, T. Shiraishi and N. Nakashima, *Chem. Commun.*, 2016, **52**, 12972–12975.
20 J. A. Robinson, E. S. Snow, S. C. Badescu, T. L. Reinecke and F. K. Perkins, *Nano Lett.*, 2006, **6**, 1747–1751.
21 M. Kim, C. Chen, P. Wang, J. J. Mulvey, Y. Yang, C. Wun, M. Antman-Passig, H.-B. Luo, S. Cho, K. Long-Roche, L. V. Ramanathan, A. Jagota, M. Zheng, Y. Wang and D. A. Heller, *Nat. Biomed. Eng.*, 2022, **6**, 267–275.
22 C. Wagner, *Ann. Rev. Mater. Sci.*, 1977, **7**, 1–22.
23 A. Puntambekar, N. Chandrasekeran, Q. Wang, I. Roy, V. Premkumar and V. Chakrapani, *ACS Appl. Energy Mater.*, 2018, **1**, 3093–3102.
24 C. T. White, D. H. Robertson and J. W. Mintmire, *Phys. Rev. B: Condens. Matter Mater. Phys.*, 1993, **47**, 5485–5488.
25 S. Kilina and S. Tretiak, *Adv. Funct. Mater.*, 2007, **17**, 3405–3420.
26 H. Kwon, A. Furmanchuk, M. Kim, B. Meany, Y. Guo, G. C. Schatz and Y. Wang, *J. Am. Chem. Soc.*, 2016, **138**, 6878–6885.
27 M. J. Frisch, G. W. Trucks, H. B. Schlegel, G. E. Scuseria, M. A. Robb, J. R. Cheeseman, G. Scalmani, V. Barone, G. A. Petersson and H. Nakatsuji, *Gaussian 09*, Gaussian Inc., Wallingford, CT, USA, 2013.
28 M. J. Frisch, G. W. Trucks, H. B. Schlegel, G. E. Scuseria, M. A. Robb, J. R. Cheeseman, G. Scalmani, V. Barone, G. A. Petersson and H. Nakatsuji, *Gaussian 16*, Gaussian Inc., Wallingford, CT, USA, 2016.
29 J. V. Lill, G. A. Parker and J. C. Light, *Chem. Phys. Lett.*, 1982, **89**, 483–489.
30 R. Dennington, T. A. Keith and J. M. Millam, *GaussView, 6.0.16*, Semichem Inc., Shawnee Mission, KS, USA, 2016.
31 X. Wu, M. Kim, H. Qu and Y. Wang, *Nat. Commun.*, 2019, **10** 2672.
32 H. Qu, A. Rayabharam, X. Wu, P. Wang, Y. Li, J. Fagan, N. R. Aluru and Y. Wang, *Nat. Commun.*, 2021, **12**, 310.
33 C. Allard, L. Alvarez, J.-L. Bantignies, N. Bendiab, S. Cambré, S. Campidelli, J. A. Fagan, E. Flahaut, B. Flavel, F. Fossard, E. Gaufrès, S. Heeg, J.-S. Lauret, A. Loiseau, J.-B. Marceau, R. Martel, L. Marty, T. Pichler, C. Voisin, S. Reich, A. Setaro, L. Shi and W. Wenseleers, *Chem. Soc. Rev.*, 2024, **53**, 8457.

